Computers, Materials &
Continua

Tech Science Press

https://doi.org/10.32604/cmc.2026.081791

ARTICLE

Unveiling the Electronic and Optoelectronic Properties of Pure, Point-Defective, and Isovalent Ru-Doped OsI_2 Monolayer: Defect Recovery from First Principles

Vipin Kumar (विपिन कुमार)[1,*] and Pushpendra Kumar[2]

[1]Department of Electronics and Communication Engineering, School of Engineering, SR University, Warangal, Telangana, India
[2]Department of Physics, Manipal University Jaipur, Jaipur, Rajasthan, India

*Corresponding Author: Vipin Kumar. Email: kumar.vipin118@gmail.com

Received: 09 March 2026; Accepted: 06 May 2026; Published: 15 June 2026

ABSTRACT: In this paper, we report the effects of point defects and doping on the physical properties of the two-dimensional OsI_2 monolayer. A point defect was created by removing a single Os/I atom from the perfect crystal lattice of the OsI_2 monolayer. For doping, we use an isovalent Ru element from the transition-metal family. Point defects and doping alter the band structure by creating new localized electronic states within the gap. Moreover, the electronic bands show a shift due to point defects. However, changes in the bandgap due to point defects and doping are not remarkable. This suggests that isovalent Ru doping is favorable in the OsI_2 crystal lattice for the formation of other similar hybrids. Moreover, the isoelectronic substitution of the Ru atom at the Os vacancy contributes to defect recovery. The dielectric and optical properties of the point-defect OsI_2 monolayer change significantly at low energies. For instance, the dielectric function abruptly changes in the infrared (IR) region in the presence of the Os and I vacancies, significantly altering the optical absorption. A sudden increase in the dielectric constant increases the material's refractive index (4.04), which is slightly greater than that of silica (3.9). The obtained reflection and transmission spectra demonstrate that these materials are potential candidates for anti-reflective coatings, as they exhibit reflectivity below 25% across the IR, visible, and ultraviolet regions. The pure and Ru-doped materials exhibit excellent static reflectivity below 4%, whereas the defective OsI_2 monolayers exhibit reflectivity below 6%. Furthermore, all the optical responses in these materials are polarization-dependent, indicating anisotropic behavior under the incident light field. The observations in this work show that these are excellent anisotropic optical materials with potential for use in optical instruments and optoelectronic device applications.

KEYWORDS: Two-dimensional dihalides; electronic properties; optical properties; optoelectronics; density functional theory

1 Introduction

The unprecedented preparation of atomically thin graphene [1] has opened a frontier for materials scientists seeking 2D counterparts of other known bulk materials, using advanced experimental tools. Until now, several 2D nanomaterials have been synthesized and characterized for various potential applications. For instance, MXenes [2,3], transition metal dichalcogenides (TMD) [4], Janus monolayers based on TMD [5], and many more monolayers of different elements in the periodic table [6]. These 2D materials belong to a special class of ultrathin nanomaterials exhibiting exotic technological applications in various fields. For example, sensors [7], energy conversion and transistors [8,9], optical [10,11], and optoelectronic devices [12,13], including image detection through localization effects. Few TM-based dichloride materials have been reported as excellent candidates for technological applications in the semiconductor industry due to their exotic electronic and mechanical properties [14,15]. Some transition-metal dihalides (TMDHs) have also been investigated for spintronic applications because they exhibit excellent magnetic properties [16,17]. Owing to the unusual physical and chemical properties of low-dimensional materials, 2D transition-metal halide compounds have attracted considerable research interest for their exceptional optoelectronic properties [18]. Specifically, transition-metal dihalide (TMDH) compounds are the most important family members of 2D materials. The crystal structure of TMDH in low dimensions exhibits a one-dimensional (1D) chain or layers in a 2D plane [19]. Several stable and exfoliable TMDHs have been reported to show tunable magnetic ordering in 2D dimensions [20]. The crystal structures and properties of various 2D TMDH materials were also explored theoretically [21,22]. Many 2D TMDHs have also been screened using high-throughput computational and machine-learning techniques and are now available in databases [23].

The TMDHs have a general chemical formula of MX_2, where M represents a transition metal, and X represents a halogen. These can also be thought of as the composition of a 3D transition metal and a halogen atom. These have layered crystal structures in their bulk form. Van der Waals interactions between layers are responsible for their layered structures. The TMDHs have several compositional possibilities involving transition-metal and halogen atoms and feature a large bandgap [24]. These materials have also been successfully synthesized using various experimental techniques, including epitaxial growth and physical and chemical vapor deposition. Homogeneous magnetic layers of $FeCl_2$ and $NiCl_2$ TMDHs have been successfully grown epitaxially via molecular sublimation on a metallic Au(111) substrate, demonstrating their scalability and potential for integration into spintronic devices [24]. Physical and chemical vapor deposition techniques synthesize few-layer and monolayer NiI_2 on an h-BN substrate, exhibiting ferroelectricity and inversion-symmetry-breaking magnetic order [25]. Another study shows that the grown NiI_2 nanostructure exhibits multiferroicity at the atomic scale [26]. Recently, Fe-based dihalide nanostructures were synthesized by reducing trihalides [16]. Other TMDH nanomaterials have also been synthesized using various methods [16,27,28].

The above discussion shows that TMDHs have been explored for applications ranging from nano spintronics to optoelectronics. They exhibit layer-dependent, tunable properties from the bulk to the monolayer. These studies are conducted on pure TMDH materials, ranging from bulk to monolayer forms. Low-dimensional TMDHs with exotic properties have significant potential for technological development. OsI_2 is also a member of the 2D TMDH family. It is an unexplored 2D material within the family of 2D TMDHs with potential applications in electronic and optoelectronic devices. A first-principles study of the $RuOsSe_2$ hybrid monolayer reveals its potential for optoelectronic applications in the visible and ultraviolet (UV) regions [29]. A recent survey of the thermodynamically stable pure osmium diiodide (OsI_2) monolayer reveals that it can absorb visible and UV radiation and exhibits optical anisotropy [30]. The Os-based halide and chalcogenide compounds and hybrids are explored for various properties in their pure form. However, the effects of doping and vacancy on the properties of TMDHs have not been reported. This motivates us to further explore the electronic and optical properties of the engineered OsI_2 monolayers for possible device applications. The structural modifications were achieved through vacancy (point defect) and doping effects. Therefore, we investigated the effects of vacancies and point defects, including Ru doping, on the electronic and optical properties of the OsI_2 monolayer using computational tools. We use an isovalent Ru substitution in the host OsI_2 monolayer. The host (Os) and the dopant (Ru) have similar atomic radii and are isovalent. Because of the isovalent nature of Ru and its similar atomic radii to those of the host Os, the Ru can easily be incorporated in the OsI_2 crystal lattice. Hence, Ru can form analogous compounds to those of Os. It is expected that the isovalent Ru substitution at the Os vacant site in the host material will contribute to defect recovery. This article is arranged in the following sections. Section 1 describes the motivation and background of the problem under discussion. It provides insights into related works from a literature survey. Section 2 presents the simulation strategy and calculation details. The results of the first-principles DFT calculations are presented in Section 3. Finally, we have summarized our results in Section 4.

2 Computational and Calculation Details

We investigated the properties of the OsI_2 monolayers using the OpenMX simulation code [31], which is based on density functional theory (DFT) [32,33], norm-conserving pseudopotentials [34], and pseudo-atomic localized basis functions [35,36]. The structural parameters (internal coordinates and cell vectors) of the OsI_2 monolayer were fully optimized and relaxed with the self-consistent field (SCF) iterative and molecular dynamic (MD) approach using the variable cell optimization scheme without constraint, which combines rational function (RF) [37], direct inversion iterative subspace (DIIS) [38], and Broyden-Fletcher-Goldfarb-Shanno (BFGS) [39–42] methods. The SCF iterations continue until the energy convergence criterion is met, which is equal to or less than 10^{-7} Hartree. The force optimization criterion during MD steps was set to 3×10^{-4} Hartree/Bohr. A regular $7 \times 7 \times 1$ mesh of k points was used during the geometry optimization. Optimized pseudoatomic basis functions, listed in Table 1, were considered to expand the Kohn-Sham wave functions [35]. The used cutoff radius for both Os- and I-atom is 7.0 Bohr. The kinetic energy cutoff of 240 Ry was chosen to solve the Poisson equation [43]. The Brillouin zone (BZ) is sampled with a $7 \times 7 \times 1$ k-point mesh for numerical integration. The density of states was calculated using a large $35 \times 35 \times 1$ k-point mesh. It has been well-tested that the optical quantities calculated with the OpenMX code are independent of the k-grid points [31]. Here, we use a regular $21 \times 21 \times 1$ mesh of k points to calculate the dielectric and optical quantities. The OpenMX calculates the dielectric and conductivity tensors using the Kubo-Greenwood formula [44]. These quantities were calculated in the linear optical response. Here, it is worth mentioning that only the direct optical transitions are considered in the present calculations. This means that all phonon-assisted optical transitions are forbidden. Moreover, the calculated dielectric and optical quantities do not include many-body effects as well [45,46].

Table 1: List of used optimized pseudoatomic basis functions.

Element	Os	I	Ru
Basis function	Os7.0-s3p2d2	I7.0-s3p2d2f1	Ru7.0-s3p2d1

3 Results and Discussions

3.1 Optimized Crystal Structures

The structural formula of the osmium diiodides is of the OsI_2 type, similar to other well-known transition metal dihalides (TMDHs) [20,21]. It crystallizes in two different phases: hexagonal (2H, space group $p\bar{6}m2$) and trigonal (1T, space group $p\bar{3}m1$). The optimized crystal structures of the 1T phase of the pure, point-defective (Os/I vacancy), and Ru-doped OsI_2 monolayers are illustrated in Fig. 1. In the onward discussion, these systems are denoted by OsI_2:pure, OsI_2:V_{Os}, OsI_2:V_I, and OsI_2:Ru, Fig. 1a–d, respectively. The side view of the OsI_2 monolayer is shown in Fig. 1e. The primitive cell of the OsI_2 monolayer is shown as a red-dashed parallelogram in Fig. 1a. The Os and I atoms are shown in silver and pink, respectively. The monolayer OsI_2 possesses a trigonal symmetry and belongs to a space group number 164 ($p\bar{3}m1$). In its crystal structure, each central Os atom is octahedrally coordinated to six nearest-neighbor I-type atoms, forming two sublayers on either side, Fig. 1e. A $3 \times 3 \times 1$ supercell of 2D OsI_2 monolayer is prepared by the repetition of the single unit cell three times along the in-plane ***a*** and ***b*** directions, respectively. The lattice constant of the optimized $3 \times 3 \times 1$ supercell containing 27 atoms (nine Os and eighteen I) of 2D OsI_2:pure monolayer is a = b = 12.17 Å. The crystal lattice parameters obtained are similar to those of transition metal 27 atoms (nine Os and eighteen I) as reported in the 2D material database [47]. Additionally, the calculated lattice constant of OsI_2 is comparable to those of other reported TMDH monolayer materials [20,21]. The calculated lattice constant of the single OsI_2 unit cell and Os-Os and Os-I distances agree with the reported values [30].

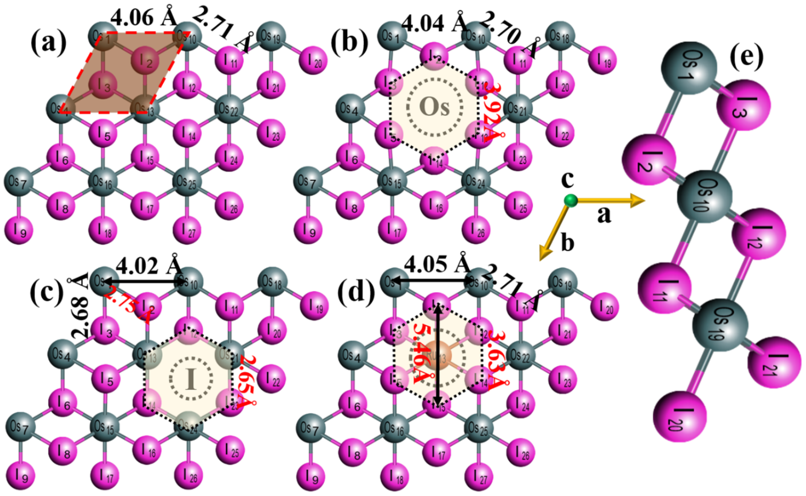

Figure 1: Optimized crystal structures of OsI_2:pure (**a**), OsI_2:V_{Os} (**b**), OsI_2:V_I (**c**), and OsI_2:Ru (**d**). (**e**) shows the side view. The circle shows the vacancy/dopant sites.

These crystal lattice parameters slightly deviate in the point-defective (Os/I vacancy) and Ru-doped OsI_2 monolayer. The created Os and I vacancies, which are a type of point defect, are shown as dashed circles in Fig. 1b,c. Alternatively, these point defects can be the missing of an atom from one of the crystal lattice sites. These point defects in the OsI_2 monolayer slightly decreased the lattice constant in the OsI_2:V_{Os} and OsI_2:V_I systems; see Fig. 1b,c, respectively. The lattice constants (e.g., the Os-Os distance) of OsI_2:V_{Os} and OsI_2:V_I are reduced to 4.04 Å and 4.02 Å, respectively. The Os vacancy in the OsI_2 monolayer gives rise to a hexagonal-type vacant region with I atoms at all corners of the hexagon, shown in Fig. 1b. In contrast, Os and I atoms are situated alternatively on the corners of the hexagon in the OsI_2 with an I vacancy, shown in Fig. 1c. The I-I distance around the vacant Os site in the OsI_2:V_{Os} is 3.92 Å, as depicted in Fig. 1b, whereas the Os-I distance around the vacant I site in the OsI_2:V_I is 2.65 Å, as depicted in Fig. 1c. The Ru-doped site in the OsI_2:Ru monolayer is also indicated by a dashed circle, as shown in Fig. 1d. A single Ru atom is inserted at one of the equivalent vacant Os sites by substitutional doping, which corresponds to the 3.70% doping of Ru in a 3 × 3 × 1 supercell of the OsI_2 monolayer. The Ru substitutional doping can also be considered an Os-vacancy filler, as it is clear from Fig. 1b,d. The lattice constant of the OsI_2:Ru monolayer is 4.05 Å. The I-I distance around the dopant site, shown by a hexagon in Fig. 1d, is 3.63 Å, and the Ru-I distance is 2.73 Å, which is slightly greater than the Os-I distance at the dopant site in the pure material. It may be attributed to the difference in atomic radii between the removed Os atom and the inserted Ru atom. It is important to note that the atomic radii of Os and Ru are 185 and 178 pm, respectively. The dopant Ru has a smaller atomic radius than the Os atom, leading to an increase in the Ru-I distance (2.73 Å) than the Os-I distance (2.71 Å); thereby slightly decreasing the lattice constant of OsI_2:Ru compared to that of the pure material.

The structural and energetic stability of these OsI_2 systems was verified by calculating their cohesive energies. It is the amount of energy required to separate the constituent atoms in a solid crystal into their free state of neutral atoms. The cohesive energies (E_C) were calculated using the following formula

$$E_C = \frac{E_{OsI_2} - E_{Os} - E_I}{n_{Os} + n_I} \tag{1}$$

In Eq. (1), E_{OsI_2} is the total energy of the OsI_2 monolayer, E_{Os} and E_I are the total energies of the isolated Os and I atoms, respectively, whereas n_{Os}/n_I is the number of Os/I atoms. According to the mathematical expression of the cohesive energy in Eq. (1), its more negative value indicates the most energetically favorable structure. The obtained cohesive energies of the OsI_2:pure, OsI_2:V_{Os}, OsI_2:V_{Os}, and OsI_2:Ru are −4.33, −4.16, −4.31, and −4.30 eV, respectively. These are also listed in Table 2. The pure OsI_2 monolayer has a more negative value of the cohesive energy. It is the most energetically stable structure, indicating the formation of strong chemical bonds between Os and I atoms. It results in the stronger interaction between Os and I atoms in the OsI_2:pure, indicating a short bond length compared to those with a less cohesive energy of −4.30 eV in the OsI_2:Ru, Fig. 1a,d. However, the stability of other materials is slightly reduced, indicating elongation of chemical bond lengths, thereby weakening the bonds. It is generally believed that a high cohesive energy in a geometrical structure usually implies a lower total energy of the corresponding material, indicating energetically favorable crystal structures. Moreover, cohesive energies are also affected by the geometry of the crystal structure. The calculated cohesive energies suggest that these structures are stable and energetically favorable to form. Additionally, the high cohesive energy of these structures indicates that they are mechanically strong. In other words, the geometrical structures with a high cohesive energy possess a high mechanical strength. Furthermore, the phonon dispersion of the OsI_2 monolayer exhibits its dynamical stability due to the absence of negative phonon frequencies, as reported by others [30].

Table 2: Lists the optimized lattice parameters of the considered 2D OsI_2 monolayers in the 3 × 3 × 1 supercell. The lattice parameters reported in the other work correspond to a single unit cell. The cohesive energy is also listed.

Material	**OsI_2:pure**	**OsI_2:V_{Os}**	**OsI_2:V_I**	**OsI_2:Ru**
Lattice parameters (this work), a = b (Å)	12.17, 4.03 [29]	12.15	12.06	12.17
$d_{Os\text{-}Os}$ (Å)	4.06	4.04	4.02	4.05
$d_{Os\text{-}I}$ (Å)	2.71	2.70	2.68	2.71
E_C (eV)	−4.33	−4.16	−4.31	−4.30

3.2 *Effect of Point Defect and Doping on the Electronic Properties of the OsI_2 Monolayer*

Here, the Kohn-Sham electronic band structure and density of states (DOS) were discussed to investigate the electronic behavior of the OsI_2 monolayers. In the Kohn-Sham approximation, the band structure is the set of energy eigenvalues as a function of wave vector. The Kohn-Sham electronic band structure was calculated along the high symmetry paths (Γ-M-K-Γ) of the first BZ. Fig. 2a,b shows the band structure and DOS of OsI_2:pure monolayer. In the valence band (VB) and conduction band (CB), there is a set of energy bands separated by a finite energy gap. For instance, there are two sets of bands in the VB and CB, spanning −4.0 to 0.0 eV and 0.5 to 4.0 eV, respectively. The subbands in the VB are separated by a gap of 0.61 eV, where the top and bottom of the lower and upper subbands lie at the K and Γ-points of the BZ. Similarly, the bottom and top of the upper and lower subbands in the CB lie along the Γ-M path and at the Γ-point, respectively. These subbands in the CB are separated by 1.08 eV. The bottom of the lower subband and top of the upper subband in the CB and VB are located between the Γ and M points, exhibiting a bandgap of about 1.20 eV. Thus, the 2D OsI_2:pure monolayer is a direct bandgap semiconductor for a range of k-values (in Bohr^{-1}) between 0.1063 and 0.1122. It exhibits a direct bandgap of about 1.27 and 1.34 eV at M- and K-points, respectively. The obtained bandgap is comparable to the reported value using the PBE functional [30]. However, the GGA-PBE underestimates [48] the bandgap value due to the involved self-interaction error in treating the exchange-correlation energy. This difficulty in determining the bandgap can be overcome by using a hybrid functional (such as HSE06) for the exchange-correlation. We employed the OpenMX DFT code to calculate the physical properties of the 2D OsI_2 monolayer, which does not include HSE06 functionality. Therefore, we reported all the results in the present study using the PBE functional. The obtained bandgap of OsI_2:pure monolayer can be verified with the total density of states (TDOS), as shown in Fig. 2b. There are zero available DOS near the Fermi level within the energy range −0.61 to +0.59 eV, indicating a bandgap of 1.20 eV between the VB and CB.

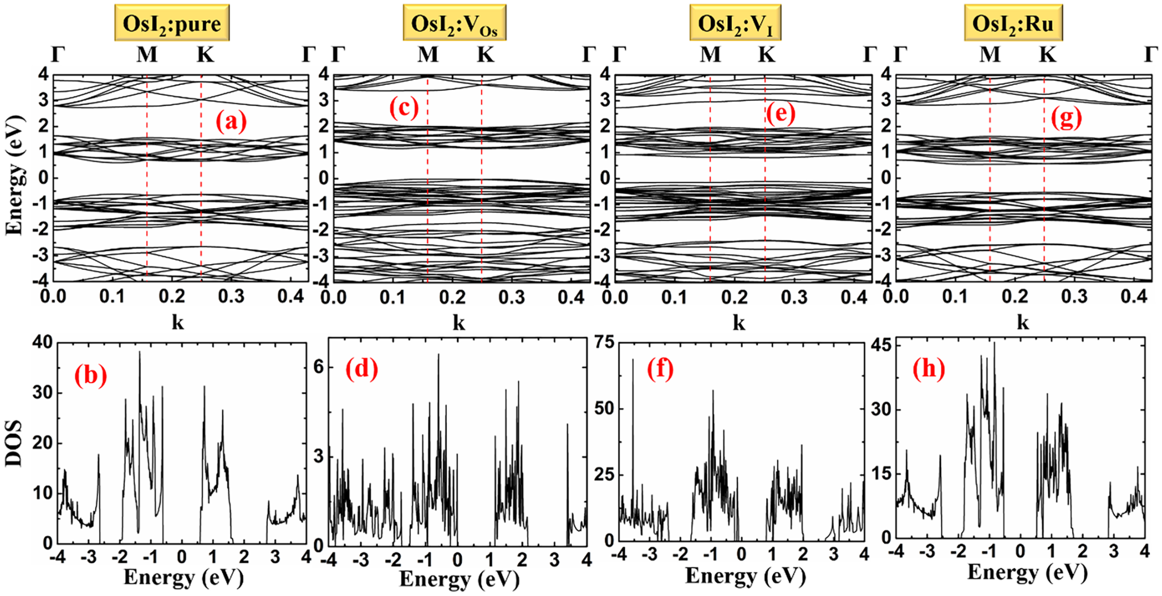

Figure 2: Electronic band structure of (**a**) OsI_2:pure, (**c**) $OsI_2:V_{Os}$, (**e**) $OsI_2:V_I$, and (**g**) OsI_2:Ru monolayers. Their density of states is shown in (**b**,**d**,**f**,**h**), respectively. The Fermi level is set at the zero-energy level.

Electronic properties can be significantly altered by point defects such as vacancies (missing atoms) and by doping, both of which fall within the scope of the present discussion. In the present study, two types of vacancy were created: one by removing a single Os atom and the other by removing a single I atom from the crystal structure of the OsI_2 monolayer. These systems are referred to as the $OsI_2:V_{Os}$ (Os-point defect/vacancy) and $OsI_2:V_I$ (I-point defect/vacancy), respectively, and are shown in Fig. 1b,c, respectively. The electronic band structure of the $OsI_2:V_{Os}$ monolayer is illustrated in Fig. 2c. Like the OsI_2:pure monolayer, two subbands in the VB and CB can be observed in the $OsI_2:V_{Os}$ monolayer. These subbands are separated by a gap of 0.22 and 1.21 eV in the VB and CB, respectively. Now, the top of the VB (−0.02 eV) is at the M-point of the BZ, and the bottom of the CB (+1.16 eV) is still lying in the Γ-M path of the BZ. Thus, a single Os vacancy negligibly changes the band gap of the OsI_2 monolayer. Moreover, the whole electronic structure is observed to be slightly shifted compared to that of the pure material due to the shifting of the Fermi level caused by the presence of dangling bonds or unpaired electrons (due to the missing Os atom). Comparing the band structures of the pure and Os vacancy-defected OsI_2 monolayer, it is evident that the vacancy leads to more electronic bands to appear, e.g., new localized energy levels, in the VB and CB, which are solely attributed to the single vacancy defect (or the point defect/missing atom). This point defect creates localized defect energy levels close to the band edges, forming shallow donor and acceptor levels that shift the Fermi level. In particular, the Os point defect in the OsI_2 monolayer creates localized electronic energy states near the top of the VB. It shifts the Fermi level close to the VB. These changes in the electronic structure, due to electron deficiency caused by a point defect (e.g., an Os vacancy), can significantly modify a material's optical response. The change in the band structure of the OsI_2 monolayer with an Os point defect is clear from the DOS; see Fig. 2d. The appearance of additional localized electronic DOS is evident from Fig. 2d. These localized energy states can be attributed solely to the Os point defect, i.e., the missing single Os atom from one of the crystal lattice sites of the pure host material.

An explanation similar to that for the Os point defect can also be applied to the I vacancy defect to explain the electronic properties of the OsI_2 monolayer. As with the Os point defect, two subbands are observed in VB and CB, as shown in Fig. 2e. In the I point defect, shallow and deep localized defect energy levels are observed both close to and far from the VB and CB edges, resulting in a shift in the Fermi level position due to the presence of the point defect. A nearly flat band in the electronic band structure of OsI_2:V_I is observed at the top and bottom of the VB and CB, respectively. Alternatively, these flat bands occur in the gap region of the OsI_2 monolayer, and they are solely attributed to the I point defect, a missing I atom from one of the crystal sites in the host material. Similar to the Os vacancy, the Fermi level shifted towards the VB for a single I vacant position in the OsI_2 monolayer. These changes in electronic band structure due to the I-point defect can be corroborated with the DOS, as shown in Fig. 2f. The localized electronic energy levels within the bandgap are evident due to the I-point defect in the OsI_2 monolayer. Similar to the Os point defect, the I point defect has almost a negligible effect on the bandgap of the OsI_2 monolayer.

Next, we discuss the effect of Ru-doping on the band dispersion of the OsI_2 monolayer. This Ru doping can also be considered a filler for the Os vacancy in the OsI_2:V_{Os} monolayer. Its band structure and DOS are shown in Fig. 2g,h. It is observed that Ru doping introduces new localized electronic states into the band structure. In the Ru-doped OsI_2 monolayer, there are two subbands in the VB and CB, as in the pristine material. The upper and lower subbands in the VB and CB appear at energies between −0.54 and −1.91 eV and +0.73 and +1.73 eV, respectively. Additionally, two energy bands below the bottom subband in the CB are evident in the energy range between +0.53 and +0.71 eV and are solely attributed to Ru doping. Unlike p- or n-type doping, Ru-doping does not introduce free electronic charge carriers because it is isoelectronic (or isovalent) with the host atom; it does not add or remove free carriers such as electrons or holes. In other words, isovalent doping is considered in the present case to recover vacancies. A slight band edge shifting in the VB and CB is observed due to the difference in the atomic radii of the host Os (185 pm) and Ru dopant (178 pm) atoms. The difference in atomic radii can also slightly distort the crystal lattice locally. Moreover, a direct band gap of approximately 1.03 eV, at the k value of 0.115 Bohr^{-1}, can be achieved due to the occurrence of the intermediate localized energy bands below the CB minimum. However, a direct bandgap of approximately 1.07 eV is observed at the M-point of the BZ. The energy difference between the VBM at the k value of 0.115 Bohr^{-1} and at the M-point is nearly 0.03 eV, which is very small. Therefore, the Ru-doped OsI_2 can also be considered as a Quasi (semi)-direct bandgap semiconductor at the M-point of the BZ, which is similar to that observed in the 2D hexagonal SnTe monolayer [49]. The DOS corroborates the band structure of OsI2:Ru; see Fig. 2h. New electronic states are evident in the DOS plot, arising from Ru substitutional doping at an Os site in the OsI_2 crystal lattice. The doping-induced or impurity energy levels can be identified in Fig. 2h near the bottom of the CB. These impurity energy levels also appear deep in the VB and the CB, as shown in Fig. 2h.

The DOS projected on the constituent Os and I atoms is depicted in Fig. S1 of the Supplementary Material (SM). The Os atom has a dominant contribution to the total DOS in both the VB and CB. The VB below the Fermi level is mainly populated by the Os atom, Fig. S1a–d of the SM. The I atom contributes less to the total DOS. However, a slight degree of hybridization is also observed in the Ru-doped OsI_2 monolayer. The impurity electronic energy levels below the bottom of the CB are evident as sharp peaks in the DOS of OsI_2:Ru, as shown in Fig. S1d. Moreover, a few impurity levels due to Ru doping also appear in the top

VB subband below the Fermi level, as shown in Fig. S1d. All the discussion above shows that point defects (vacancies) can significantly modify the electronic properties, thereby altering the dielectric and optical responses of the OsI_2 monolayer. Moreover, the isoelectronic substitution of the Ru atom at the Os vacancy contributes to defect recovery in the OsI_2:V_{Os} monolayer. This means that isoelectronic Ru substitutional doping at the Os site recovers almost all the electronic properties of the pure OsI_2 monolayer. A similar phenomenon has also been reported in the rhenium diselenide ($ReSe_2$) monolayers in the presence of various kinds of point defects [50]. Therefore, we have also systematically studied the effects of point defects and isoelectronic doping on the dielectric properties and the optical responses of the OsI_2 monolayer, as discussed in the sections below.

The defect and doping cause a redistribution of electronic charge. The calculated net charge on each atom in the OsI_2:pure configuration is shown in Fig. S2 of the SM. It can be noticed that each Os and I atom in an intrinsic OsI_2 monolayer has a net electronic charge of about −0.355 and +0.177, respectively. This means that each Os atom can accept 0.355 electrons from the two bonded I atoms, each I atom having a net charge of about 0.177. In other words, each I atom has electron donor features, while each Os atom acts as an electron acceptor. However, this electronic distribution is disrupted by point defects and substitutional doping. This means the electronic redistribution occurs in the presence of point defects created by removing an atom from a crystal lattice site. For instance, the change in the electronic distribution in the presence of the Os vacancy is shown in Fig. S3 of the SM. It can be noticed that the effect of the Os vacancy significantly affects the electronic charges on other atoms throughout the crystal lattice. All the I atoms nearest to the vacant Os site now have a reduced electron-donating capability, down to 0.054 electrons compared to 0.177 electrons in the pure OsI_2 monolayer. The next-nearest neighbor of the same type as the vacant site is also significantly affected, showing a slightly reduced electron-accepting feature. A similar effect on the electron-donating and accepting features can also be noticed in the presence of an I vacancy in the OsI_2 monolayer, as shown in Fig. S4 of the SM. Here, the electronic charge on each nearest I atom is slightly increased, indicating these nearest I atoms to the vacant I site have more electron-donating capability. At the same time, however, the electron-accepting capability of the nearest Os atom to the vacant I site is slightly reduced. The effect of isoelectronic Ru doping on the electronic distribution of the OsI_2 monolayer is shown in Fig. S5 of the SM. It is observed that the Ru doping at one of the equivalent Os sites in the OsI_2 crystal lattice significantly changes the electronic charges on each nearest bonded I atom. The electronic charge on each nearest I atom bonded to the Ru atom is now reduced to +0.137 from its value +0.177 in the pure OsI_2 monolayer, indicating a reduced electron-donating feature. However, the Ru atom can accept about 0.153 electrons from surrounding atoms. The electronic charges on the nearest Os atoms to the Ru-doping site are not significantly affected. However, the next-nearest I atoms have a slightly higher electronic charge than in the pure OsI_2 monolayer.

These changes in electronic distribution, caused by point defects and doping, lead to differences in the electron density between the considered monolayer materials, as shown in Fig. S6 of the SM. From Fig. S6a, it can be observed that most of the difference electronic density is uniformly concentrated around the Os atoms, with yellow and blue indicating electron-rich and electron-deficient regions, respectively, and the amount is negligible at each I site. This difference electron density distribution is disturbed in the presence of the point defect (Os/I vacancy); see Fig. S6b,c for the Os and I vacancy, respectively. For instance, the Os/I vacancy leads to a change in the difference electron density around the Os/I atoms; see Fig. S6b,c. However, the change in the difference electron density due to the Os vacancy in the OsI_2 monolayer can again be recovered by isovalent Ru substitution, as shown by comparing Fig. S6a,d. This indicates that isoelectronic Ru doping acts as a defect-recovery agent, suggesting the successful formation of various Os- and Ru-based dihalide/chalcogenide hybrids, similar to the $RuOsSe_2$ hybrid [29]. Fig. 3 shows the total spectral weights and the orbital-projected spectral weights in the materials under investigation. For instance, the green circles in Fig. 3a,d,g,j show the total spectral weights, while solid black curves show the conventional band structure obtained from the DFT calculations. On the contrary, Fig. 3b,c,e,f,h,i,k,l shows the orbital decomposed band structures (orbital projected spectral weights) of the constituent elements in the OsI_2:pure, $OsI_2:V_{Os}$, $OsI_2:V_I$, and OsI_2:Ru monolayers, respectively. Red is the spectral weight of the 's' orbitals, green is the spectral weight from the sum of all 'p' orbitals, blue is the spectral weight from the sum of all 'd' orbitals, and magenta is the spectral weight from the sum of all 'f' orbitals. The radius of circles reflects the magnitude of the spectral weight. The Os-d orbital has made a predominant contribution to the top of the VB in all materials, while a slightly less contribution in forming the CBM. These observations are consistent with the atom-projected DOS shown in Fig. S1a for the pure material, as reported in the SM. However, it is the Ru-d orbital that makes a predominant contribution near the VBM and the CBM (Fig. 3k), consistent with the atom-projected DOS shown in Fig. S1d of the SM. Moreover, the hybridization between the transition metal's 'd' orbital and halogen (I) 'p' orbital is obvious from the middle and the right columns panel.

3.3 Effect of Point Defect and Ru-Doping on the Dielectric and Optical Properties

The material's dielectric response is an intrinsic property and varies from material to material. In other words, it demonstrates the material's ability to be polarized due to the shifting of electric charges in the presence of an applied field. This phenomenon enables the determination of the material's permittivity (dielectric constant). The material's dielectric response depends on factors such as its composition, physical state, and the frequency of the applied field. A material with a higher permittivity exhibits a stronger response to light. The frequency dependence of the dielectric response makes it a complex quantity. It can be expressed as $\epsilon(\omega) = \epsilon_1(\omega) + i\,\epsilon_2(\omega)$. Here, the $\epsilon_1(\omega)$ and $\epsilon_2(\omega)$ are the frequency-dependent real and imaginary parts of the complex dielectric function. The real part indicates the material's polarizability and its dispersion of light. It demonstrates the material's ability to store electrical energy. In contrast, light absorption (or extinction) is governed by the imaginary part, as the light travels through the material, and it contains all the information about electronic transitions. The mathematical expression of the $\epsilon_2(\omega)$ is as follows [51,52]

$$\epsilon_2(\omega) = \frac{4\pi^2 e^2}{Vm^2\omega^2}\sum_{nn'}\langle kn|p_i|kn'\rangle\langle kn'|p_j|kn\rangle f_{kn}(1-f_{kn'})\,\delta(E_{kn'}-E_{kn}-\hbar\omega) \tag{2}$$

In Eq. (2), e and m are the electronic charge and mass, V is the unit cell volume, p is the momentum operator, $|kn\rangle$ is the wave function with an eigenvalue of E_{kn}, and f_{kn} is the Fermi distribution function. However, the Kramer-Kronig transformation calculates the real dielectric function [53] as follows

$$\epsilon_1(\omega) = 1 + \frac{2}{\pi}\boldsymbol{P}\int_0^{\infty}\frac{\omega'\,\epsilon_2(\omega)\,d\omega'}{\omega'^2-\omega^2} \tag{3}$$

The frequency-dependent optical parameters, such as absorption $(\alpha(\omega))$, extinction $(\kappa(\omega))$, transmission $(T(\omega))$, and reflection $(R(\omega))$ coefficients can easily be calculated, including the refractive index, $n(\omega)$, and energy loss function, $L(\omega)$, can be calculated as follows.

$$\alpha(\omega) = \frac{\omega}{\sqrt{2}}\left(\left[\epsilon_1^2(\omega)+\epsilon_2^2(\omega)\right]^{\frac{1}{2}} - \epsilon_1(\omega)\right)^{\frac{1}{2}} \tag{4}$$

$$\mathrm{n}(\omega) = \frac{1}{\sqrt{2}}\left(\left[\epsilon_1^2(\omega)+\epsilon_2^2(\omega)\right]^{\frac{1}{2}} + \epsilon_1(\omega)\right)^{\frac{1}{2}} \tag{5}$$

$$\kappa(\omega) = \frac{1}{\sqrt{2}}\left(\left[\epsilon_1^2(\omega)+\epsilon_2^2(\omega)\right]^{\frac{1}{2}} - \epsilon_1(\omega)\right)^{\frac{1}{2}} \tag{6}$$

$$R(\omega) = \frac{(n(\omega)-1)^2 + k^2(\omega)}{(n(\omega)+1)^2 - k^2(\omega)} \tag{7}$$

$$L(\omega) = \frac{\epsilon_2(\omega)}{\epsilon_1^2(\omega) - \epsilon_2^2(\omega)} \tag{8}$$

where all other symbols have their usual meaning.

The calculated frequency-dependent imaginary dielectric function and the absorption coefficient for OsI_2 monolayers are illustrated in Fig. 4. The material's linear response in the visible and ultraviolet (UV) regions is indicated in the blue and green double-headed arrow at the top of each plot. The material's response to the light field is indicated by the x ($\mathbf{E}||x$) and z ($\mathbf{E}||z$) components in each plot. From Fig. 4, it can be noticed that the material's in-plane responses to the incident light field are the same. This means that the material exhibits an in-plane isotropic response to the light field, e.g., the in-plane components of $\epsilon_2(\omega)$ overlap; see Fig. 4a. Therefore, only the x component of the material's in-plane response is shown in all plots. The in-plane components of all studied physical quantities are illustrated in red and blue throughout the manuscript. From the imaginary dielectric response of all materials, along with their band structures and DOS, the different electronic transitions between the VB and CB can be identified. The $\epsilon_2(\omega)$ in the OsI_2:pure monolayer is shown in Fig. 4a. The $\epsilon_2(\omega)$ exhibits different maxima at photon energy of 1.78, 2.40, and 4.58 eV for the x-component. However, the z-component exhibits a maximum at 1.73, 4.81, 5.71, and 6.76 eV, respectively. The onset of $\epsilon_2(\omega)$, and the entire spectrum is slightly shifted towards the ultraviolet (UV) region, for the $\mathbf{E}||z$ than that of the $\mathbf{E}||x$. However, the onset of $\epsilon_2(\omega)$ for both components belongs to the infrared (IR) region of electromagnetic radiation. The x-component of $\epsilon_2(\omega)$ exhibits a maximum at the interface of the visible and UV regions, which is entirely in the UV region for $\mathbf{E}||z$. It indicates that the OsI_2:pure monolayer exhibits significant visible-light absorption for $\mathbf{E}||x$; see Fig. 4b. In contrast, most of the light absorption along the z-direction occurs in the UV region, Fig. 4b. The onset of light absorption for both components is in the IR region, at 0.83 eV ($\mathbf{E}||x$) and 1.30 eV ($\mathbf{E}||z$); see Fig. 4b. The OsI_2:pure monolayer exhibits significant light absorption in the UV region for both components due to carrier transitions between occupied and unoccupied states in the VB and CB, Fig. 4b, as is clear from the electronic band structures.

The dielectric response of the OsI_2 monolayer in the presence of a point defect (Os and I vacancy) is shown in Fig. 4c,e, while the corresponding absorption coefficient is illustrated in Fig. 4d,f. It can be observed that the OsI_2 monolayer exhibits markedly different dielectric response and light absorption in the presence of point defects. In both cases, the $\epsilon_2(\omega)$ exhibits a peak (x-component) in the low-energy IR region, which was absent in the pure OsI_2 monolayer, e.g., the point defect shifts the peak to lower energy. This feature is solely attributable to defect states in the OsI_2 monolayer due to Os and I vacancies, which modify electronic transitions. In the presence of vacancies, the entire spectrum of the $\epsilon_2(\omega)$ for the z-component is shifted towards the higher energy compared to the x-component. However, the peaks around 5.0 eV ($\mathbf{E}||x$) and 7.0 eV ($\mathbf{E}||z$) are intact in all cases, which lie in the UVC region. Light absorption is significantly increased in the UV region in the presence of point defects (Os and I vacancies), as shown in Fig. 4d,f, respectively. The increased absorption in the defective OsI_2 monolayer can be explained as follows. The periodic potential is disrupted by defects, leading to localized electronic energy levels within the gap region. These defect energy levels within the bandgap allow electrons to excite themselves at lower photon energies. It leads to a redshift of the material's absorption edges, which expands the absorption energy range; hence, a broader range of wavelengths can be absorbed by the material. In other words, the created defect sites act as additional photon-absorption centers. It increases the material's photon capture ability, thereby enhancing light absorption in the defective OsI_2 Monolayer. Their higher absorption indicates that these are potential UV absorbers, similar to the 2D magnesium dihalides [54,55].

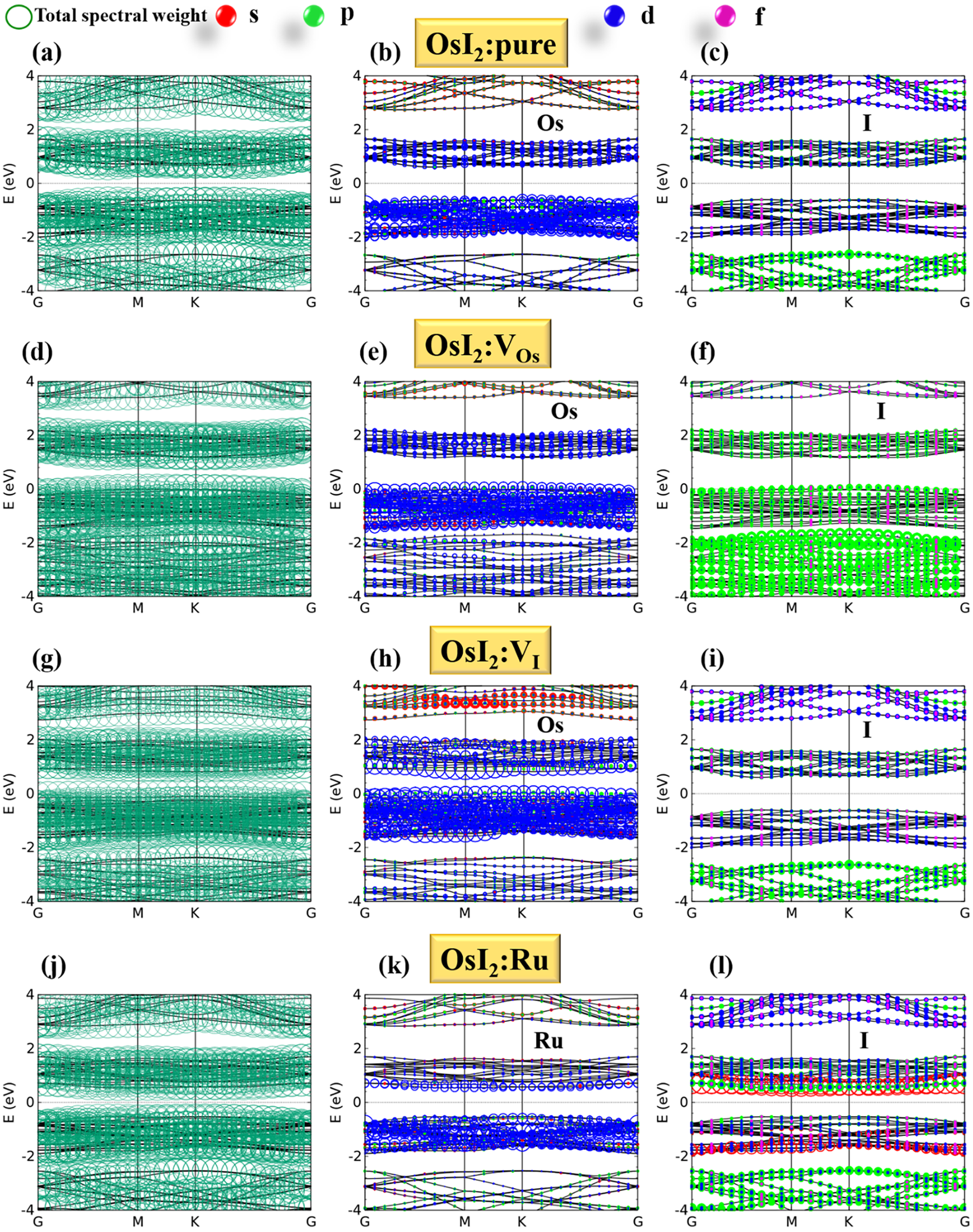

Figure 3: Solid lines show the band structures from the conventional DFT calculations, and the green circles in the left column (Figs. (**a**,**d**,**g**,**j**)) panel are the total spectral weight. Orbital decomposed contributions to the band structure from the constituent atoms (Os/Ru) (Figs. (**b**,**e**,**h**,**k**)) and (**I**) (Figs. (**c**,**f**,**i**,**l**)). Red, green, blue, and magenta show the spectral weights from the s, p, d, and f orbitals, respectively.

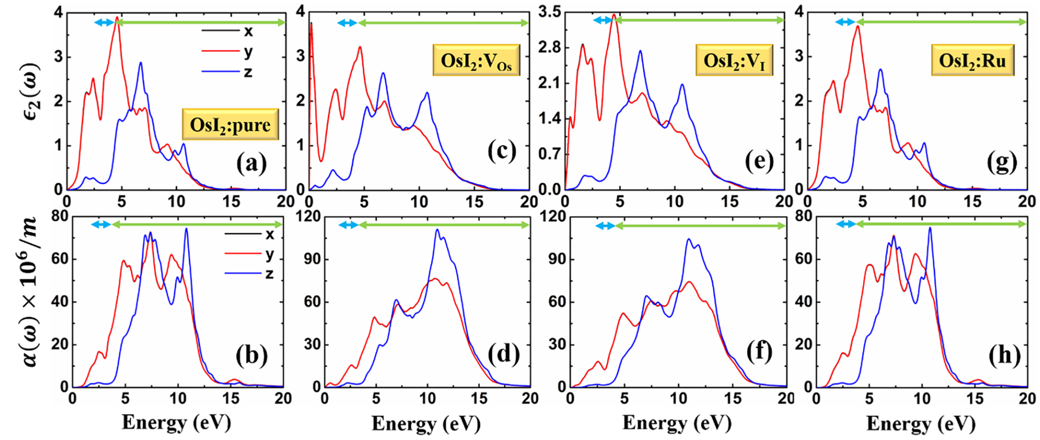

Figure 4: The imaginary part of the dielectric function and absorption coefficient in the OsI$_2$:pure (**a**,**b**), OsI$_2$:V$_{Os}$ (**c**,**d**), OsI$_2$:V$_I$ (**e**,**f**), and OsI$_2$:Ru (**g**,**h**), respectively. The blue and green double arrows in each plot indicate the visible and ultraviolet regions.

The effect of doping on the $\epsilon_2\ (\omega)$ and the absorption coefficient, $\alpha(\omega)$, on the OsI$_2$ monolayer is elucidated in Fig. 4g,h, respectively. The onset of $\epsilon_2\ (\omega)$ and $\alpha(\omega)$ exhibits a redshift, e.g., the low-energy response is shifted to lower energies due to a slight reduction in the bandgap caused by Ru-doping at one of the equivalent Os sites in the host OsI$_2$ monolayer. As mentioned earlier, Ru doping slightly distorts the host crystal lattice, thereby changing the electronic band structure; in particular, a slightly reduced bandgap is observed. It slightly changes the fundamental absorption edges, and a redshift is seen in both the $\epsilon_2\ (\omega)$ and $\alpha(\omega)$ of the OsI$_2$:Ru. It is worth mentioning here that the host and dopant are both isovalent. An isovalent dopant can control the intrinsic point defect. However, the host Os (185 pm) and dopant Ru (178 pm) have a small atomic radius difference of 7 pm. Hence, the host crystal lattice does not deform much. It can also lead to the formation of a new composite material similar to RuOsSe$_2$ [29]. The change in the absorption edges is due to intermediate localized impurity electronic states induced by isovalent Ru doping in the OsI$_2$ monolayer. Therefore, it is seen that the Ru can easily be incorporated into the OsI$_2$ crystal lattice due to its isovalent nature and similar atomic radii to those of the host Os. After the Ru substitutional doping at the Os vacant site in the OsI$_2$:V$_{Os}$ monolayer, the material exhibits properties similar to those of the pure OsI$_2$ monolayer. This means that isoelectronic Ru doping at one of the Os-vacant sites in the OsI$_2$ monolayer almost recovers the changes induced by the Os vacancy. Therefore, the isoelectronic substitution of the Ru atom at the Os vacancy contributes to defect recovery. All the considered materials exhibit significant light absorption across the visible to the UV region, with a small absorption in the IR region as well. Hence, these materials are excellent absorbers across a wide range of wavelengths in the electromagnetic spectrum, from the IR to the visible to the UV region, demonstrating their potential for optoelectronic device applications.

The extinction coefficient, $\kappa(\omega)$, for these materials is shown in Fig. S7 of the SM. The extinction coefficient is closely related to the absorption coefficient. It quantifies the loss of intensity due to absorption. However, the $\kappa(\omega)$ is the total light attenuation; it is generally the sum of absorption and scattering. The material's higher extinction coefficient means that it absorbs light more effectively, e.g., the light photons strongly interact, which are quickly absorbed by the material. In other words, the material's higher extinction coefficient shows higher light absorption (see Fig. S7 of the SM). The peak position in the extinction coefficient occurs nearly at the same energies as that of the absorption coefficient. Therefore, the calculated extinction coefficient is consistent with the absorption spectrum of the materials under consideration. A material's higher extinction coefficient can have potential applications in the sensitivity detection. Additionally, both the imaginary dielectric function and the absorption coefficient behave differently for different orientations of the light field. This means that both are anisotropic in response to the photon field. However, this anisotropy in these quantities is prominent only in the IR-to-visible-to-UV region; for energies above 15.0 eV, all the considered OsI_2 monolayers exhibit isotropic behavior. This suggests that it can be useful for polarization-dependent optical instruments and devices. Energy losses are always associated with light absorption and extinction. The average energy losses are shown in Fig. S8 of the SM. It is observed that most of the energy losses are concentrated around 11.38 and 13.54 eV for pure (Ru-doped) and point-defective OsI_2 monolayers, respectively, indicating that light absorption and extinction are prominent in the UV region. The maxima in the loss spectrum corresponds to plasma resonances, and the associated frequency is called the plasma frequency.

Next, we discuss the frequency-dependent real dielectric function, $\epsilon_1\ (\omega)$, and the refractive index, $n(\omega)$, in the defective and doped OsI_2 monolayers, as illustrated in Fig. 5. The real dielectric function indicates the material's ability to store the electrical energy, which shows the material's ability to be polarized by the field. It can also be thought of as the induced internal field opposes the changes inside the material due to the external field. At the same time, the frequency-dependent refractive index quantifies the bending or slowing of light when it enters the material. The $\epsilon_1\ (\omega)$ is related to the phase velocity; however, the $n(\omega)$ determines the amount of light refraction or the bending of light when it enters the material. The calculated $\epsilon_1\ (\omega)$ in an intrinsic OsI_2 monolayer (OsI_2:pure) is shown in Fig. 5a. The most important is the static dielectric constant, $\epsilon_1\ (0)$, which is the value of the real dielectric constant at zero photon energy. For OsI_2:pure, the $\epsilon_1\ (0)$ is nearly 4.05 and 2.15 along the $\mathbf{E}||$x- and $\mathbf{E}||$z. The $\epsilon_1\ (0)$ in an intrinsic OsI_2 monolayer is slightly higher than that of the standard value of the silica (3.9) [56], demonstrating its applications as a gate dielectric. It increases smoothly with increasing photon energy, reaching its peak values of 4.91 and 3.22 at 1.24 and 4.32 eV for $\mathbf{E}||$x and $\mathbf{E}||$z, respectively. These peak values indicate that the material is strongly polarized due to the applied field. At these energies, the frequency of the applied field matches the material's natural oscillation frequency, e.g., the resonant frequency of the bound charges within the material, thereby increasing the amplitude of the oscillating charges and giving rise to a sharp peak in the real dielectric function, Fig. 5a. The induced polarization is strongly in phase with the electric field below the resonance. However, this phase was disrupted by further increasing the photon frequency, resulting in a decrease in $\epsilon_1\ (\omega)$. A sharp drop in the $\epsilon_1\ (\omega)$ is observed, after its peak value at 1.24 eV, with further increasing photon frequency. It is due to the phase lag in the induced polarization with the external field. It demonstrates that the material's ability to store electrical energy decreases as photon frequency increases. Therefore, Fig. 5a shows that the intrinsic OsI_2 monolayer exhibits better performance for storing electrical energy in the IR region, with a continuous decrease in the visible and UV regions. It also shows a slight negative value at specific photon energies, demonstrating its metallic character at those energies. It is due to the opposite orientation of the induced dielectric displacement to the applied field, exhibiting an unusual material's polarization in response to the external field. It is a useful property for creating superlenses. On the other hand, the z-component exhibits a wide energy range for storing electrical energy across the far IR-to-visible-to-low-energy-UV region. Moreover, the different behavior of the real dielectric function under different light polarization directions again shows that the material exhibits anisotropy. However, this anisotropy disappears at energies above 12.0 eV.

The real dielectric function, $\epsilon_1\ (\omega)$, is significantly affected in the defective OsI_2 monolayer due to the presence of a point defect (Os/I vacancy). The effect of the point defect, the Os and I vacancy, on the $\epsilon_1\ (\omega)$ in the pristine OsI_2 monolayer (OsI_2:pure) is depicted in Fig. 5c,e, respectively. The static dielectric constants of Os and I-defective OsI_2 monolayers are significantly increased in comparison to the intrinsic ones. The observed value of the $\epsilon_1\ (0)$ in the OsI_2:V_{Os}, Fig. 5c, and OsI_2:V_I are approximately 9.78 and 6.03, respectively. Therefore, the Os and I vacancies in the OsI_2 monolayer not only enhance the dielectric constant but also give rise to a high-k dielectric feature. Hence, both OsI_2:V_{Os} and OsI_2:V_I are useful for realizing electronic devices based on high-k dielectric materials. Also, their higher dielectric constant indicates that they are more suitable than intrinsic materials for storing electrical energy and can be more strongly polarized by the light field. However, the static dielectric constant of the OsI_2 monolayer is not significantly affected by these point defects along the z-direction, which is approximately 2.53 and 2.41 for OsI_2:V_{Os} and OsI_2:V_I, respectively. The static dielectric constants are listed in Table 3. An induced depolarization effect is also observed in both materials, leading to a sharp drop in the $\epsilon_1\ (\omega)$ with increasing photon frequency, as shown in Fig. 5c,e. The Ru-doping slightly alters its static value relative to its intrinsic value; see Fig. 5g. The $\epsilon_1\ (0)$ in the OsI_2:Ru is 4.15 and 2.19 for **E**||x and **E**||z, respectively. Again, the effect of Ru-doping does not deviate much from the response of the real dielectric function in comparison to that of the intrinsic response. This is due to the isoelectronic (or isovalent) nature and similar atomic radii of the dopant Ru and host Os atoms, which suggest that Ru doping can be readily incorporated into the preparation of different hybrids without significantly altering their physical properties. It reveals that Ru substitutional doping at one of the Os vacant sites in the OsI_2:V_{Os} monolayer contributes to the defect recovery, yielding optical responses similar to those of the pure and Ru-doped OsI_2 monolayers.

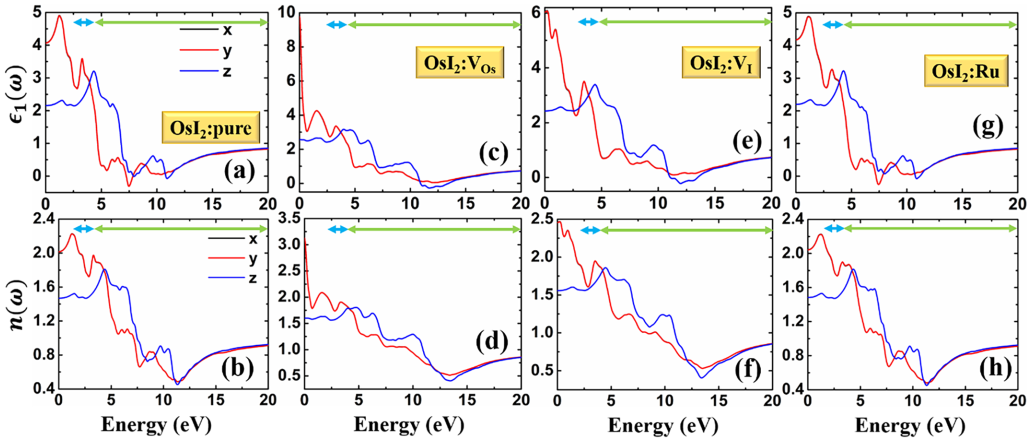

Figure 5: The real part of the dielectric function and refractive index of the OsI_2:pure (**a**,**b**), OsI_2:V_{Os} (**c**,**d**), OsI_2:V_I (**e**,**f**), and OsI_2:Ru (**g**,**h**), respectively. The blue and green double arrows in each plot indicate the visible and ultraviolet regions.

Table 3: Static real dielectric constants of an intrinsic and defective OsI_2 monolayer along different orientations of the light field.

Material	OsI_2:pure		OsI_2:V_{Os}		OsI_2:V_I		OsI_2:Ru	
$\epsilon_1\ (0)$	E||x	E||z	E||x	E||z	E||x	E||z	E||x	E||z
	4.05	2.15	9.78	2.53	6.03	2.41	4.15	2.19

Refractive index is another important parameter of an optical material. It is the quantity that determines the bending of light when it enters a medium of a different refractive index. It is a material-dependent and intrinsic property. It also depends on the wavelength and is generally a complex function. Thus, it can be expressed as, $\overline{n}\ (\omega) = n\ (\omega) + i\kappa(\omega)$. Here, the real part represents the refractive index, which quantifies the bending of light. The imaginary part is the extinction coefficient, which accounts for light absorption in the medium and was discussed earlier and shown in Fig. S7 of the SM. The static refractive index, $n(0)$, is its value at the zero energy of the incident photon field. It is an important measure for a material to be applied in various optical and optoelectronic instruments and devices. It can be determined as $n(0) = \sqrt{\epsilon_1(0)}$. The static refractive indices of OsI_2:pure, $OsI_2:V_{Os}$, $OsI_2:V_I$, and OsI_2:Ru monolayers are 2.02 (1.46), 3.13 (1.59), 2.46 (1.55), and 2.04 (1.48), respectively, for x(z)-components of the light polarization. It can be noticed that the static refractive index of the OsI_2 monolayer is enhanced significantly in the presence of point defects (Os and I vacancy). It is the maximum for the $OsI_2:V_{Os}$ among all the materials studied, indicating that the speed of light is affected much and slowed down when it enters the $OsI_2:V_{Os}$ than that of the intrinsic material. In other words, the $OsI_2:V_{Os}$ monolayer is a strongly refracting material among other studied materials, and hence, exhibits more light bending. This property of the point defect in the OsI_2 monolayer can be utilized to manipulate the light propagation through it. Moreover, a less light refraction is observed for the z-component in all materials.

The refractive index increases from its static value as the photon frequency increases. For instance, the x-component of the refractive index in OsI_2:pure increases from its static value of 2.02 to 2.23 at 1.27 eV in the IR region, Fig. 5b. In contrast, the z-component shows a maximum refractive index of 1.82 at 4.38 eV. These static values (listed in Table 4) are slightly higher than those reported for the 2D magnesium dihalides [54,55]. The refractive index of all the studied materials shows a sharp decrease after their first maximum as the photon frequency increases, Fig. 5b,d,f,h for OsI_2:pure, $OsI_2:V_{Os}$, $OsI_2:V_I$, and OsI_2:Ru monolayers, respectively. The reason behind a sharp decrease in refractive index is also the same as in the case of the real dielectric function, as already discussed above. The refractive index of the intrinsic and Ru-doped OsI_2 monolayer is approximately the same, again emphasizing that it is due to the isovalent doping in the host material. It also suggests that the Ru-doping contributes to defect recovery in the $OsI_2:V_{Os}$ monolayer. Moreover, as mentioned earlier, the atomic radii of the host and dopant are also similar, differing by 7 pm. It leads to a less-distorted crystal lattice in the host material, resulting in behavior that is almost the same. It is another indication of the successful incorporation of Ru into the host lattice without significant changes in its properties, demonstrating the formation of various hybrids. However, a thorough experimental study is needed to verify it, which is beyond the scope of the present work. Moreover, the refractive index is polarization-dependent, indicating an anisotropic response to light fields with different polarization directions. This anisotropy, however, disappears for energies greater than 15.0 eV. Therefore, the materials studied exhibit birefringence. Hence, these materials are birefringent, exhibiting double refraction. The incident light is split into two rays: the mutually perpendicular ordinary and the extraordinary rays. They travel at different speeds due to the differences in the refractive index. The difference between the refractive indices is called the birefringence, as shown in Fig. S8 of the SM. It can be noticed that all materials exhibit negative birefringence below 5.0 eV and positive birefringence above it, which are related to the material's optical anisotropy. The negative birefringence implies that the refractive index of the medium in the direction of propagation of an ordinary ray is greater than that of the propagation direction of an extraordinary ray. This is the reason why extraordinary light waves travel faster than ordinary light waves. However, in the case of positive birefringence, the speed of the ordinary light wave is greater than the speed of the extraordinary light wave. It is an important phenomenon with applications in liquid crystal displays for light control and image creation. Optical waveplates exploit this phenomenon to control and modify the polarization state of light (e.g., from linear to circular and *vice versa*). In materials science, it is used to identify and study crystal lattice structures.

Table 4: Static refractive index of an intrinsic and defective OsI_2 monolayer along different orientations of the light field.

Material	**OsI_2:pure**		**OsI_2:V_{Os}**		**OsI_2:V_I**		**OsI_2:Ru**	
$n(0)$	**E**||x	**E**||z	**E**||x	**E**||z	**E**||x	**E**||z	**E**||x	**E**||z
	2.02	1.46	3.13	1.59	2.46	1.55	2.04	1.48

The calculated percentage reflection and transmission coefficients of the materials under consideration are presented in Fig. 6 as a function of energy. It can be observed from Fig. 6a,g that the static light reflection (static reflection coefficient, R(0)) along the $x(z)$-direction is below 12% (4%) for the pure and Ru-doped OsI_2 monolayers, respectively. An overall reflection coefficient of less than 25% in the IR-to-visible-to-UV region indicates their potential as antireflective coating materials, as shown in Fig. 6a,g. However, the corresponding static transmission coefficients, T(0), are greater than 87% (97%) for **E**||x(z) in the pure and Ru-doped OsI_2 monolayers; see Fig. 6b,h, respectively. However, the obtained transmission coefficient remains above 75% over the energy range 0–20 eV. Hence, these materials may be useful for polarization-dependent light transmission filters. The static reflection coefficients in the defective OsI_2 monolayer, with a point defect of Os and an I vacancy, are slightly increased compared to those of the pure and doped monolayer. The Os and I vacancies result in static reflection coefficients of less than 27% and 18%, respectively, as shown in Fig. 6c,e, whereas the corresponding transmission coefficients are greater than 72% and 82%, respectively; see Fig. 6d,f. However, the average transmission is almost 85% or higher between 0 and 20 eV, indicating that these are also useful for antireflective materials in the optical and optoelectronic instruments and devices. Their reflection coefficient in the IR and visible regions is slightly higher than that observed in a few magnesium-based 2D halide materials [54,55,57]. Moreover, the reflection and transmission coefficients, after doping of the Ru atom at the vacant Os site in the OsI_2:V_{Os} monolayer, exhibit a light response similar to that of the pure material. This suggests that the isoelectronic Ru doping contributes to the vacancy recovery in the OsI_2:V_{Os} monolayer. Furthermore, the reflection and transmission coefficients of these materials depend on the polarization state of the light. This further emphasizes that these are strongly anisotropic optical materials with potential for anisotropic optoelectronic applications.

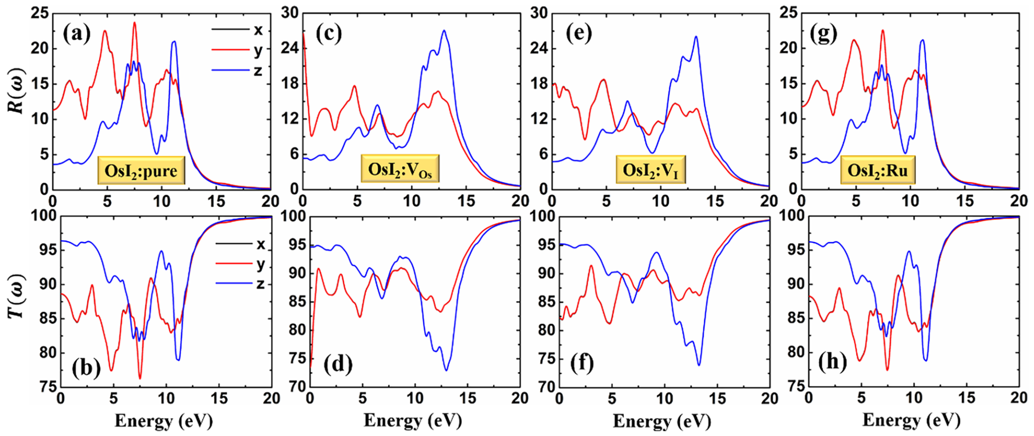

Figure 6: Reflection (**top row**) and transmission (**bottom row**) coefficients in the pure (**a**,**b**), defective (**c**–**f**), and doped (**g**,**h**) OsI_2 monolayer materials.

4 Conclusions

This work investigated the electronic and optoelectronic properties of the intrinsic, defective, and isovalent Ru-doped OsI_2 monolayer. The electronic investigations show that these are semiconducting materials. The point defect created by removing a single Os/I atom from the host crystal lattice changes the electronic band structure of the pure OsI_2 monolayer by introducing new localized electronic states in the bandgap region. A shift in the electronic bands is observed in the defective OsI_2 monolayer with respect to that of the pure material. However, the isovalent Ru-doped OsI_2 monolayer has its electronic features similar to those of the intrinsic monolayer. It is attributed to the isovalent characteristics of the Ru dopant, which has an atomic radius of 178 pm, similar to that of the host Os atom (185 pm). This small atomic-radius mismatch suggests that the doped crystal lattice of the host material undergoes only minor distortions, leading to almost no change in its electronic and, hence, optical properties. It demonstrates that isovalent Ru doping leads to the formation of hybrid materials comprising Os and Ru with potential applications in optoelectronic devices operating in the visible and UV regions. Moreover, the isoelectronic (isovalent) substitution of the Ru atom contributes to the defect recovery in the $OsI_2{:}V_{Os}$ monolayer.

However, the material's response changes remarkably in the presence of a point defect. These point-defect sites (vacancy/missing atoms) act as additional photon-absorption centers, thereby changing the response of the host material. For instance, the Os and I vacancy significantly enhances the real and imaginary dielectric responses in the infrared (IR) region. This results in an increase in the range of the absorption energy band. The dielectric constants of the Os and I vacant OsI_2 monolayers are 9.78 and 6.03 (x-components), which were nearly 4.05, slightly higher than that of the silica (3.9), for the pure and Ru-doped material. The increased dielectric constant indicates greater electrical energy storage capacity in the point-defective OsI_2 monolayers. Therefore, defective materials can be used to realize high-k dielectric materials. Additionally, it increases the refractive indices to 3.13 and 2.46 (x-component) for the Os, and I point defects in the OsI_2 monolayer, compared with 2.02 in the pure and Ru-doped material. Hence, the point-defective OsI_2 monolayers can be used in integrated optical circuits and in advanced nano-optoelectronics and photonics. Higher-refractive-index materials enable greater light confinement and improved light manipulation. The reflection and transmission spectra suggest that these are excellent antireflection coating materials, similar to those of a few magnesium dihalides, with reflectivity less than 5% in the low-energy region (IR and visible). Electronic observations indicate that the optical responses in point-defective OsI_2 monolayers are significantly enhanced. However, the isoelectronic Ru substitution at the vacant Os site in the OsI_2 monolayer restores its electronic and optical properties, e.g., acting as a defect-recovery mechanism. Therefore, the results obtained suggest that these materials are promising for optical instruments and optoelectronic devices.

Acknowledgement: Pushpendra Kumar thanks the Materials Simulation Research Center (MSRC) at Manipal University Jaipur, Jaipur, Rajasthan, for providing partial computational facilities.

Funding Statement: The authors received no specific funding for this study.

Author Contributions: The authors confirm their contributions to the paper as follows: Study conception and design: Vipin Kumar; data collection: Vipin Kumar; analysis and interpretation of results: Vipin Kumar; draft manuscript preparation: Vipin Kumar and Pushpendra Kumar. All authors reviewed and approved the final version of the manuscript.

Availability of Data and Materials: The data that support the findings of this study are available from the corresponding author, Vipin Kumar, upon reasonable request.

Ethics Approval: Not applicable.

Conflicts of Interest: The authors declare no conflicts of interest.

Supplementary Materials: The supplementary material is available online at https://www.techscience.com/doi/10.32604/cmc.2026.081791/s1.

References

1. Castro Neto AH, Guinea F, Peres NMR, Novoselov KS, Geim AK. The electronic properties of graphene. Rev Mod Phys. 2009;81(1):109–62. doi:10.1103/revmodphys.81.109.
2. Thakur A, Chandran BS, Davidson N, Bedford K, Fang A, Im H, et al. Step-by-step guide for synthesis and delamination of $Ti_3C_2T_x$ MXene. Small Meth. 2023;7(8):2300030. doi:10.1002/smtd.202300030.
3. Murali G, Reddy Modigunta JK, Park YH, Lee JH, Rawal J, Lee SY, et al. A review on MXene synthesis, stability, and photocatalytic applications. ACS Nano. 2022;16(9):13370–429. doi:10.1021/acsnano.2c04750.
4. Joseph S, Mohan J, Lakshmy S, Thomas S, Chakraborty B, Thomas S, et al. A review of the synthesis, properties, and applications of 2D transition metal dichalcogenides and their heterostructures. Mater Chem Phys. 2023;297(17):127332. doi:10.1016/j.matchemphys.2023.127332.
5. Zhang J, Jia S, Kholmanov I, Dong L, Er D, Chen W, et al. Janus monolayer transition-metal dichalcogenides. ACS Nano. 2017;11(8):8192–8. doi:10.1021/acsnano.7b03186.
6. Single-layer materials. [cited 2026 Jan 1]. Available from: https://en.wikipedia.org/wiki/2D_Materials.
7. Sulleiro MV, Dominguez-Alfaro A, Alegret N, Silvestri A, Gómez IJ. 2D Materials towards sensing technology: from fundamentals to applications. Sens Bio Sens Res. 2022;38(6):100540. doi:10.1016/j.sbsr.2022.100540.
8. Zeng S, Liu C, Zhou P. Transistor engineering based on 2D materials in the post-silicon era. Nat Rev Electr Eng. 2024;1(5):335–48. doi:10.1038/s44287-024-00045-6.
9. Zhang Q, Liu C, Zhou P. 2D materials readiness for the transistor performance breakthrough. iScience. 2023;26(5):106673. doi:10.1016/j.isci.2023.106673.
10. Kim S. All-2D material photonic devices. Nanoscale Adv. 2023;5(2):323–8. doi:10.1039/d2na00732k.
11. Zhang Y, Wu J, Jia L, Jin D, Jia B, Hu X, et al. Advanced optical polarizers based on 2D materials. npj Nanophoton. 2024;1(1):28. doi:10.1038/s44310-024-00028-3.
12. Xu H, Liu J, Wei S, Luo J, Gong R, Tian S, et al. A multifunctional optoelectronic device based on 2D material with wide bandgap. Light Sci Appl. 2023;12(1):278. doi:10.1038/s41377-023-01327-8.
13. Tang Z, Chen S, Li D, Wang X, Pan A. Two-dimensional optoelectronic devices for silicon photonic integration. J Mater. 2023;9(3):551–67. doi:10.1016/j.jmat.2022.11.007.
14. Liu D, Wang D, Zhang B, Zhao C, Liu S, He W, et al. WSe_2 interdigitated p-n homojunction for broadband high-performance imaging detection through localization effect synergizes. Adv Funct Mater. 2026;36(34):e31930. doi:10.1002/adfm.202531930.
15. Kistanov AA, Shcherbinin SA, Botella R, Davletshin A, Cao W. Family of two-dimensional transition metal dichlorides: fundamental properties, structural defects, and environmental stability. J Phys Chem Lett. 2022;13(9):2165–72. doi:10.1021/acs.jpclett.2c00367.
16. Jiang S, Wang G, Deng H, Liu K, Yang Q, Zhao E, et al. General synthesis of 2D magnetic transition metal dihalides *via* trihalide reduction. ACS Nano. 2023;17(1):363–71. doi:10.1021/acsnano.2c08693.
17. Hu L, Han J, Gao G. Layer- and barrier-dependent spin filtering effect and high tunnel magnetoresistance in $FeCl_2$ based van der Waals junctions. Appl Phys Lett. 2023;123(5):052401. doi:10.1063/5.0153195.
18. Chen Z, Xue J, Wang Z, Lu H. Magnetic hybrid transition metal halides. Mater Chem Front. 2023;8(1):210–27. doi:10.1039/d3qm00727h.
19. McGuire MA. Crystal and magnetic structures in layered, transition metal dihalides and trihalides. Crystals. 2017;7(5):121. doi:10.3390/cryst7050121.
20. Kulish VV, Huang W. Single-layer metal halides MX_2 (X = Cl, Br, I): stability and tunable magnetism from first principles and Monte Carlo simulations. J Mater Chem C. 2017;5(34):8734–41. doi:10.1039/c7tc02664a.
21. Botana AS, Norman MR. Electronic structure and magnetism of transition metal dihalides: bulk to monolayer. Phys Rev Mater. 2019;3(4):044001. doi:10.1103/physrevmaterials.3.044001.

22. Bo X, Fu L, Wan X, Li S, Pu Y. Magnetic structure and exchange interactions of transition metal dihalide monolayers: first-principles studies. Phys Rev B. 2024;109(1):014405. doi:10.1103/physrevb.109.014405.
23. Zhou J, Shen L, Costa MD, Persson KA, Ong SP, Huck P, et al. 2DMatPedia, an open computational database of two-dimensional materials from top-down and bottom-up approaches. Sci Data. 2019;6(1):86. doi:10.1038/s41597-019-0097-3.
24. Aguirre A, Pinar Solé A, Soler Polo D, González-Orellana C, Thakur A, Ortuzar J, et al. Ferromagnetic order in 2D layers of transition metal dichlorides. Adv Mater. 2024;36(28):e2402723. doi:10.1002/adma.202402723.
25. Song Q, Occhialini CA, Ergeçen E, Ilyas B, Amoroso D, Barone P, et al. Evidence for a single-layer van der Waals multiferroic. Nature. 2022;602(7898):601–5. doi:10.1038/s41586-021-04337-x.
26. Amini M, Fumega AO, González-Herrero H, Vaňo V, Kezilebieke S, Lado JL, et al. Atomic-scale visualization of multiferroicity in monolayer NiI_2. Adv Mater. 2024;36(18):2311342. doi:10.1002/adma.202311342.
27. Zhou X, Brzostowski B, Durajski A, Liu M, Xiang J, Jiang T, et al. Atomically thin 1T-$FeCl_2$ grown by molecular-beam epitaxy. J Phys Chem C. 2020;124(17):9416–23. doi:10.1021/acs.jpcc.0c03050.
28. Bikaljević D, González-Orellana C, Peña-Díaz M, Steiner D, Dreiser J, Gargiani P, et al. Noncollinear magnetic order in two-dimensional $NiBr_2$ films grown on Au(111). ACS Nano. 2021;15(9):14985–95. doi:10.1021/acsnano.1c05221.
29. Bittencourt LRP, Santos WO, Moucherek FMO, Moreira E, Barbosa LS, Azevedo DL. First-principles calculations to investigate optoelectronic and thermodynamic properties of new 1T′-$RuOsSe_2$ hybrid monolayer. Int J Mod Phys C. 2024;35(01):2450001. doi:10.1142/s0129183124500013.
30. Santos WO, Barbosa LS, Moreira E, Azevedo DL. First-principles investigation of the OsI_2 monolayer: a novel two-dimensional dihalide material for optoelectronic applications. Braz J Phys. 2024;55(1):11. doi:10.1007/s13538-024-01642-4.
31. OpenMX. [cited 2026 Jan 1]. Available from: http://www.openmx-square.org/.
32. Hohenberg P, Kohn W. Inhomogeneous electron gas. Phys Rev. 1964;136(3B):B864–71. doi:10.1103/physrev.136.b864.
33. Kohn W, Sham LJ. Self-consistent equations including exchange and correlation effects. Phys Rev. 1965;140(4A):A1133–8. doi:10.1103/physrev.140.a1133.
34. Morrison I, Bylander DM, Kleinman L. Nonlocal Hermitian norm-conserving Vanderbilt pseudopotential. Phys Rev B. 1993;47(11):6728–31. doi:10.1103/physrevb.47.6728.
35. Ozaki T. Variationally optimized atomic orbitals for large-scale electronic structures. Phys Rev B. 2003;67(15):155108. doi:10.1103/physrevb.67.155108.
36. Ozaki T, Kino H. Numerical atomic basis orbitals from H to Kr. Phys Rev B. 2004;69(19):195113. doi:10.1103/physrevb.69.195113.
37. Banerjee A, Adams N, Simons J, Shepard R. Search for stationary points on surfaces. J Phys Chem. 1985;89(1):52–7. doi:10.1021/j100247a015.
38. Császár P, Pulay P. Geometry optimization by direct inversion in the iterative subspace. J Mol Struct. 1984;114:31–4. doi:10.1016/S0022-2860(84)87198-7.
39. Broyden CG. The convergence of a class of double-rank minimization algorithms 1. General considerations. IMA J Appl Math. 1970;6(1):76–90. doi:10.1093/imamat/6.1.76.
40. Fletcher R. A new approach to variable metric algorithms. Comput J. 1970;13(3):317–22. doi:10.1093/comjnl/13.3.317.
41. Goldfarb D. A family of variable-metric methods derived by variational means. Math Comp. 1970;24(109):23–6. doi:10.1090/s0025-5718-1970-0258249-6.
42. Shanno DF. Conditioning of quasi-Newton methods for function minimization. Math Comp. 1970;24(111):647–56. doi:10.1090/s0025-5718-1970-0274029-x.
43. Ozaki T, Kino H. Efficient projector expansion for the *ab initio* LCAO method. Phys Rev B. 2005;72(4):045121. doi:10.1103/physrevb.72.045121.
44. Allen PB. Electron transport. In: Conceptual foundations of materials—a standard model for ground-and excited-state properties. Amsterdam, The Netherlands: Elsevier; 2006. p. 165–218. doi:10.1016/s1572-0934(06)02006-3.

45. Mak KF, He K, Lee C, Lee GH, Hone J, Heinz TF, et al. Tightly bound trions in monolayer MoS_2. Nat Mater. 2013;12(3):207–11. doi:10.1038/nmat3505.
46. Drüppel M, Deilmann T, Krüger P, Rohlfing M. Diversity of trion states and substrate effects in the optical properties of an MoS_2 monolayer. Nat Commun. 2017;8(1):2117. doi:10.1038/s41467-017-02286-6.
47. Fukuda M, Zhang J, Lee YT, Ozaki T. A structure map for AB_2 type 2D materials using high-throughput DFT calculations. Mater Adv. 2021;2(13):4392–413. doi:10.1039/d0ma00999g.
48. Perdew JP, Yang W, Burke K, Yang Z, Gross EKU, Scheffler M, et al. Understanding band gaps of solids in generalized Kohn-Sham theory. Proc Natl Acad Sci U S A. 2017;114(11):2801–6. doi:10.1073/pnas.1621352114.
49. Polak MP, Scharoch P, Kudrawiec R. The effect of isovalent doping on the electronic band structure of group IV semiconductors. J Phys D Appl Phys. 2021;54(8):085102. doi:10.1088/1361-6463/abc503.
50. Zhu Y, Tao L, Chen X, Ma Y, Ning S, Zhou J, et al. Anisotropic point defects in rhenium diselenide monolayers. iScience. 2021;24(12):103456. doi:10.1016/j.isci.2021.103456.
51. Delin A, Ravindran P, Eriksson O, Wills JM. Full-potential optical calculations of lead chalcogenides. Int J Quantum Chem. 1998;69(3):349–58. doi:10.1002/(SICI)1097-461X(1998)69:.
52. Karazhanov SZ, Ravindran P, Kjekshus A, Fjellvåg H, Svensson BG. Electronic structure and optical properties of ZnX (X = O, S, Se, Te): a density functional study. Phys Rev B. 2007;75(15):155104. doi:10.1103/physrevb.75.155104.
53. Fox M. Optical properties of solids. Oxford, UK: Oxford University Press; 2010.
54. Mahida HR, Patel A, Singh D, Sonvane Y, Thakor PB, Ahuja R. First-principles calculations to investigate electronic structure and optical properties of 2D $MgCl_2$ monolayer. Superlattices Microstruct. 2022;162:107132. doi:10.1016/j.spmi.2021.107132.
55. Mahida HR, Singh D, Sonvane Y, Gupta SK, Thakor PB. MgF_2 monolayer as an anti-reflecting material. Solid State Commun. 2017;252(1):22–8. doi:10.1016/j.ssc.2017.01.005.
56. Esro M, Kolosov O, Jones PJ, Milne WI, Adamopoulos G. Structural and electrical characterization of SiO_2 gate dielectrics deposited from solutions at moderate temperatures in air. ACS Appl Mater Interfaces. 2017;9(1):529–36. doi:10.1021/acsami.6b11214.
57. Kumar V, Mishra RK, Jeon H, Kumar P, Ahuja R, Gwag JS. First-principles calculations to investigate the dielectric and optical anisotropy in two-dimensional monolayer calcium and magnesium difluorides in the vacuum ultraviolet. J Phys Chem Solids. 2023;181:111482. doi:10.1016/j.jpcs.2023.111482.